Nozzle Thrust Optimization While Reducing Jet Noise

J. M. Seiner*
NASA Langley Research Center, Hampton, Virginia 23681-0001
and
M. M. Gilinsky[†]
Hampton University, Hampton, Virginia 23668

A Bluebell nozzle design concept is proposed for jet noise reduction with minimal thrust loss or even thrust augmentation. A Bluebell nozzle has a sinusoidal lip-line edge (chevrons) and a sinusoidal cross-section shape with linear amplitude increasing downstream in the divergent nozzle part (corrugations). The experimental tests of several Bluebell nozzle designs have shown noise reduction relative to a convergent–divergent round nozzle with design exhaust Mach number $M_e = 1.5$. The best design provides an acoustic benefit near 4 dB with about 1% thrust augmentation. For subsonic flow ($M_e = 0.6$), the tests indicated that the present method of design for Bluebell nozzles produces increased levels of jet noise. The proposed designs incorporate analytical theory and two- and three-dimensional numerical simulations. Full Navier–Stokes and Euler solvers were utilized. Boundary layer effects were used. Several different designs were accounted for in the Euler applications.

Nomenclature

c	= sonic velocity
c_f	= friction coefficient
c_p	= specific heat at constant pressure
c_v	= specific heat at constant volume
H_0	= total enthalpy
h_r	= radial direction step size
h_φ	= azimuthal direction step size
k	= specific heat ratio, c_p / c_v
L_0, L_n	= lip-line length of baseline and Bluebell nozzles
M	= Mach number
NPR	= nozzle pressure ratio
n_c	= corrugation frequency
n_p	= petal frequency
p	= pressure
$\boldsymbol{q}$	= velocity vector, $\boldsymbol{q}(u, v, w)$
r_+, r_-	= maximum and minimum radius values
T	= temperature
u, v, w	= velocity components in cylindrical coordinates
x, r, φ	= cylindrical coordinates
x, y, z	= Cartesian coordinates
α	= wedge or cone angle
β	= shock-wave angle
δ	= corrugation amplitude
ε	= petal amplitude
ξ, η, φ	= normalized coordinates
ρ	= density

Subscripts

c	= corrugation start
e	= nozzle exit
n	= Bluebell nozzle
0	= baseline nozzle
$*$	= critical cross section

Superscripts

0	= baseline nozzle
$*$	= boundary layer thickness

Introduction

SUCCESSFUL design of a nozzle system for supersonic commercial aircraft involves meeting both environmental and economic metrics. For nozzles, the environmental metric is noise, as expressed in the FAR 36 Stage III regulations. Economic metrics are usually associated with both takeoff and cruise aero- and propulsion performance, weight, mechanical complexity, and structural reliability. These very involved issues are beyond the scope of this paper, but there exist fundamental considerations involving implementation of both metrics that are the subject of this paper.

Several years ago, it became apparent that a program was required that placed more emphasis on scientific methods for the design of nozzles for supersonic commercial applications. Current methods heavily rely on state-of-the-art empirical methods that are supported by massive data sets from previous nozzle testing. The process is both cumbersome and expensive. Examples of this can be found in a review article by Seiner and Krejsa.[1] The most successful nozzle designs are based on nozzle geometry that controls the strength of shock waves, that can rapidly mix high- and low-speed streams efficiently, and that produce noise spectrally outside the range of the Noy weighting. One discovers very quickly, however, that real solutions can be achieved only with a nozzle concept that is still effective at reducing noise at low jet-exhaust velocities, where trades with nozzle performance are historically disappointing to date. Subsonic jet noise reduction represents a fine example of this point, where noise reduction is achieved primarily through an increase of the engine bypass ratio, which leads to low mixed-flow velocities. For supersonic aircraft, it is unknown whether an economic solution exists for high bypass ratio engines.

One simple, yet realistic, question to pose is what technology exists that can optimize both the aeroacoustic suppression characteristics and suppressed mode performance of any given nozzle design. Suppressed mode performance refers to the nozzle's efficiency with acoustic suppression devices deployed in the airflow part. One would, in particular, like to know this for nozzles targeted to operate with low jet-exhaust velocities. One cannot, of course, directly answer this question. We can, however, outline aspects of this technology. For example, in the lobed mixer of Presz,[2] counter-rotating axial vorticity generated by mixer lobes is used to mix high-speed engine primary core and fan stream flow with entrained lower speed secondary flow from an ejector inlet. The enhanced mixing is used to both increase the level of secondary flow entrainment and mix

*Senior Research Scientist. Associate Fellow AIAA.
[†]Research Professor. Senior Member AIAA.

a) Four-petal Bluebell nozzle   **b) Cross-section nozzle contour**
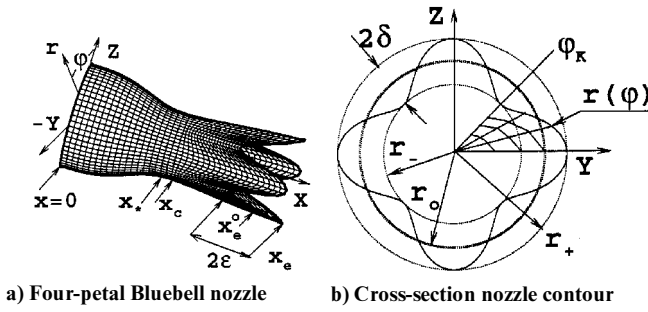
Fig. 1   Four-petal Bluebell nozzle surface geometry.

high and low stream flow to achieve lower speed uniform ejector exit velocity that has an acceptable level of external jet noise. The current state-of-the-art cannot adequately relate the design of lobe geometry to prediction of circulation strength of counter-rotating vorticity, nor can it determine the circulation strength required to achieve full mixing in the shortest possible ejector duct. Additionally, both aeroperformance computations and nozzle internal noise computations cannot be treated with accuracy sufficient to optimize the design. Similar observations of nozzle suppression effectiveness can be made for other nozzle concepts, like those previously discussed.[1]

The approach described in the present paper attempts to develop a process involving optimal design of noise-suppression technology for both subsonic and supersonic applications. As such, it is not necessary that we even consider nozzle geometry that meets any particular international noise regulation when projected to product scale. It is sufficient that the nozzle geometry selected contains one or several concepts that achieve some level of noise reduction. The long-term objective of the research is to explain observed noise reduction from alteration of the turbulent source function and relate this to the nozzle geometry for optimization. Toward this purpose, we have selected a simple axisymmetric nozzle geometry (see Fig. 1), which we denote as a Bluebell nozzle[3,4] because of the observed petal shapes of the nozzle plume generated by this nozzle. The Bluebell nozzle utilizes two concepts that have been used in the past to suppress noise. These concepts involve the use of chevrons to enhance the nozzle exit perimeter to increase the area for mixing and internal corrugations to generate counter-rotating axial vorticity to enhance mixing of high-speed primary flow with low-speed secondary flow. The present research does not yet include an ejector.

Several Bluebell nozzles have been constructed with select variations of the chevron and corrugation geometry. All of these were designed as convergent–divergent nozzles for an exit Mach number of 1.5. In this paper, predictions of thrust and measurement of the noise are made to enable optimization of the nozzle geometry. The intermediate steps of either numerical simulation or measurement of the turbulence with consequent prediction of the noise remain a deficiency of the present paper but will be addressed in future work. The thrust calculations were performed in both two and three dimensions using the Krayko–Godunov first-order numerical scheme (K-G code) with and without boundary layer corrections. In select cases, a full Navier–Stokes code with a κ-ε turbulence model, the CRAFT code, was also applied to evaluate performance-based calculations when a boundary layer correction was applied to a Euler analysis (K-G code). Acoustic measurements were acquired on baseline reference nozzles and all Bluebell nozzles. The results, as presented below, demonstrate that it is possible to achieve a level of optimal nozzle design through consideration of both performance and noise reduction. A more detailed description of the proposed approach and the results are presented.[4]

Bluebell Nozzle

Nozzle Geometry

The proposed Bluebell nozzle can be constructed on the base of any plain nozzle: axisymmetric round conical, elliptical, triangular, rectangular, or two-dimensional convergent–divergent plane. Let us consider the axisymmetric baseline nozzle contour, which is described by the function $R = R_0(x)$ in a meridional plane $\varphi = $ const.

For the Bluebell nozzle, the function $R_n(x)$ describes the nozzle geometry. The convergent part is represented by a cubic parabola, and the divergent part is calculated by using the method of characteristics (MOC).

Figure 1 shows a representative example of a four-petal Bluebell nozzle surface geometry. The x axis coincides with the nozzle axis of symmetry. The Bluebell nozzle is designed on the base of a round convergent–divergent nozzle.

A Bluebell nozzle has a sinusoidal lip-line edge, i.e., the nozzle edge distance from the nozzle throat, $x = x_e$, changes sinusoidally vs azimuth angle φ with variation in amplitude ε. The cross sections of the nozzle divergent part also are limited by sinusoidal curves vs angle φ, so that the variation amplitude in surface $r(x, \varphi)$ increases along a nozzle centerline from zero at the cross section $x = x_c$ downstream from the throat to the maximum value at the exit, $\delta = \delta_0(x - x_c)/(x_e - x_c)$. Cross section x_c is chosen to have an axial flow velocity slightly exceeding the local sound velocity ($M_x = 1.01$–1.03; details provided in the next section). Finally, the lateral surface equation of a Bluebell nozzle can be written as

$$r(x, \varphi) = R_0(x), \qquad 0 \leq x \leq x_c \tag{1a}$$

$$r(x, \varphi) = R_n(x)[1 + \delta\cos(n_c\varphi)], \qquad x_c \leq x \leq x_e(\varphi) \tag{1b}$$

$$x_e(\varphi) = x_e^0[1 + \varepsilon\cos(n_p\varphi)] \tag{1c}$$

where n_p, n_c prescribe the variation of the longitudinal lip-line change and cross section, respectively. These values are assumed to be even integers. For simplification of description, these variations are denoted as chevrons (or petals) and corrugations.

We require the same area for Bluebell and baseline nozzles in each cross section, which are denoted by $S_n(x)$ and $S_0(x)$, respectively. From this equality in cross-section area, the coordinates $R_n(x)$ are derived from Eqs. (1a–1c). A Bluebell nozzle cross-section area $S_n(x)$ is defined by the integral, which is calculated analytically. Then the function $R_n(x)$ can be expressed explicitly by baseline radius $R_0(x)$:

$$S_n(x) = \frac{1}{2}\int_0^{2\pi} r^2(x, \varphi)\,\mathrm{d}\varphi = \pi R_n^2(x)\left(1 + \frac{\delta^2}{2}\right) \tag{2a}$$

$$R_n(x) = \frac{R_0(x)}{\sqrt{1 + (\delta^2/2)}} \tag{2b}$$

Here it is assumed that $R_0(x) = R_0(x_e^0)$ for $x > x_e^0$.

A divergent part lateral surface area and a lip-line length in general can be calculated numerically only for the table data $R_0(x)$. For some particular cases, these values can be defined analytically. For example, a lip-line length of a Bluebell nozzle without petals ($\varepsilon = 0$) is expressed by elliptical functions and, additionally, if it is assumed that $\delta = 1$, the appropriate integral is defined by the elementary functions. A lateral surface area S_n can be defined analytically for conical nozzles with divergent angle α, so that $R_0(x) = 1 + \tan \alpha$ $(x - x_*)$. The corresponding integral can also be expressed by elementary functions. We write this formula for a nozzle with petals without corrugations ($\delta_0 = 0$):

$$S_n = (\pi x_e^0 / \cos \alpha)(2 + x_e^0 \tan \alpha + \tfrac{1}{2}x_e^0 \varepsilon^2 \tan \alpha) \tag{3}$$

Note that the cross-section equivalent radius of a Bluebell nozzle $R_n(x)$ is independent of frequency n_c, and the lip-line length increases with both n_p and n_c as well as the lateral surface area. For small values of ε and δ, this increase is small. Calculations show that the lip-line length ratios L_n/L_0 are more dependent on δ than lateral area ratios. The lateral area ratios are close to one for small values of δ. This is very important for practical applications to minimize wall friction effects.

Another Bluebell nozzle embodiment is based on the MOC-designed round nozzle with extended cylindrical pipe ($r = R(x_e^0)$ at $x > x_e^0$). Such a design provides a more uniform pressure distribution at the lip-line edge and this reduces the barrel shock intensity in the jet exhaust. In particular, a nozzle with petals, but without corrugations ($\delta_0 = 0$), is a shock-free nozzle. In this case, such a design has less thrust than that corresponding to the first embodiment.

Theory, Numerical Methods

Theoretical Approach

The general purpose of the theoretical approach is to define the optimum conditions that provide minimum Bluebell nozzle thrust loss by comparison with the baseline convergent–divergent design, or conical nozzles. To achieve an optimal nozzle design, the solution would require multiple computations of a three-dimensional supersonic flow region. For practical applications, unit Reynolds numbers are very high ($Re = 10^6$–10^8). Under these conditions, the boundary layer at the wall is turbulent. Its value makes up a small portion (~ 1–3%) of the cross-sectional size. For example, in accordance with Ref. 5, the ratio of the local boundary layer thickness $\delta*$ to the distance x along a flat plate is dependent on the local Reynolds number, Re_x, as given by the relationship

$$\delta*/x = 0.02 \times Re_x^{-\frac{1}{7}} \tag{4a}$$

The local wall skin friction coefficient $c_f = \tau_w/(\frac{1}{2}\rho_\infty U_\infty^2)$ is given by

$$c_f = 0.0263 \times Re_x^{-\frac{1}{7}} \Big/ \{1 + [(k-1)/4]M_\infty^2\}^{\frac{5}{7}} \tag{4b}$$

In such a situation, it is inefficient to use a numerical solution based on the full unsteady Navier–Stokes equations. Our approach is based on the viscous–inviscid interaction.[5] We used the Euler Approximation for definition of the external inviscid flow outside a thin boundary layer whose thickness is defined by Eq. (4a) with friction along the nozzle wall defined by Eq. (4b). The Euler calculations were repeated for each new nozzle shape ($r = R_1$) after accounting for the boundary layer thickness ($\delta*$), i.e., $R_1(x, \varphi) = R(x, \varphi) - \delta*(x, \varphi)$. The new computed external inviscid flow again was used for definition of a new boundary layer thickness. In each iteration, of course, the boundary layer is computed at the given nozzle surface $r = R(x, \varphi)$. Usually, the results were closed after several (three or four) iterations.

Subsonic and transonic flow numerical simulation in the convergent nozzle part was conducted in the interval $0 \le x \le x_c$ by an implicit upwind second-order numerical scheme (ENO version) for solution of the full unsteady Navier–Stokes equations, as incorporated in the CRAFT code of CRAFT-Tech (see Ref. 6). This code was originally developed by Molvik and Merkle.[7] The algorithm, its capability, and several modifications with different applications are described in a set of papers by Dash et al. (see, for example, Ref. 6). Thus, we omit its description completely. We modified this code so that, in some time intervals of the Euler stage computation, we could adapt Patankar–Spalding's code[8] for boundary layer computation. With this code, we made a correction of the nozzle boundary location and then continued computation by the CRAFT code. Such a procedure is repeated until two consequent iterations differ by less than a given small value. Note also that in most of our computations, the problem is two dimensional, because we are able to assume that in this interval the nozzle is axisymmetric. Recall that the cross section x_c is chosen to have an axial flow velocity slightly exceeding the local sound velocity ($M_x = 1.01$–1.03). Several variants of completely three-dimensional problems were computed by this method using the CRAFT-Spalding combination code. We used that only for comparison and examination of the main approach results obtained by two- and three-dimensional marching schemes. The grid at the Bluebell nozzle surface is shown in Fig. 1a. It is based on the cylindrical coordinate system, which transforms to the normalized (ξ, η, φ) system, so that in the x and r directions the computational region becomes a unit square in ξ, η variables ($0 \le \xi \le 1, 0 \le \eta \le 1$).

Krayko–Godunov Numerical Scheme

Numerical simulation of supersonic flow in the divergent nozzle part and exhaust jet was conducted by the Krayko–Godunov explicit first-order numerical scheme (K-G code).[9] Consider a cylindrical coordinate system (x, r, φ), as shown in Fig. 1a, with components of velocity-vector q on these axes of (u, v, w), and let q be a modulus of velocity-vector q, p be a pressure and ρ be a density. All variables are nondimensional. Linear sizes are related to throat radius r_*

velocities to sound velocity c_* in the nozzle critical section (throat), density to the critical density ρ_*, and pressure to $\rho_* c_*^2$. The gas is assumed perfect with constant specific heat coefficients c_p and c_v, so that specific heat ratio $k = c_p/c_v$ is constant. The Euler equation is written in the form of the integral conservation laws:

$$\frac{d}{dx} \iint_\Sigma a\, dr\, d\varphi = \oint_L (c - a\varsigma^\varphi)\, dr - (b - a\varsigma^r)\, d\varphi + \iint_\Sigma f\, dr\, d\varphi \tag{5}$$

where vectors a, b, c, and f are the usual conservation variables (see Refs. 4 and 9 for details); L is some reserved contour, which limits the area Σ in an arbitrary cross section, $\varsigma = dn/dx$, where dn is a projection of displacement L to an outward normal. Vectors ς and dn are perpendicular to the x axis in each point of contour L. They are completely defined by their projections ς^r and ς^φ to the r and φ axes. The equation for a total enthalpy conservation, H_0, written along with Eq. (5), completely defines the system.

Three-dimensional fixed grids are used. In plane r, φ the region contained within external flow boundary $R(\varphi)$ in the r direction and between two symmetry planes $\varphi = 0$, $\varphi = \pi/n_c$ in the φ direction are split by K radial straight lines $\varphi = $ const and J lines $\xi = $ const as shown in Fig. 1b. The η lines contain straight intervals between appropriate splitting points of neighboring radial lines. A splitting in the φ direction (h_φ) is chosen uniform, and in the r direction (h_r) it is a geometric progression with a denominator that is defined by equality of the neighbor cell sizes at both sides of each boundary. This provides uniform accuracy for numerical results near boundaries, which can represent shock waves, slip shocks, or usual streamline surfaces. The step size h_r increases near the axis of symmetry.

The known flow values at cross section $x = x_i$ will define those in the following section $x_{i+1} = x_i + h_x$. For each cell (as control volume) we write the conservation laws (5) using the usual explicit first-order finite differential scheme, which includes the conservation variable values at the lateral cell sides. These values are designated by capital letters A, B, C and they correspond to the similar small conservative values a, b, c for cell centers of the cross sections x_i, x_{i+1}.

Big values are used to determine the elementary solutions by considering the similar two-dimensional steady problem of two uniform unlimited interacting supersonic flows. Depending on the relational flow direction, the pressure and density ratio from different locations and combinations of the shock waves, uniform flow regions, slip shocks, and rarefaction waves were obtained. We can consider such an interaction problem by assuming that flows in the neighboring grid cells are uniform at each cell interface. There are five main possible mutual locations of the cell interface and similar flow regions.[9] Determined values correspond to the similar solution in one of the regions. These solutions require iterations. Linear (acoustics) approximation (Riemann solver) allows us to avoid these iterations. However, such an approach does not provide the necessary accuracy of numerical solution, and in some cases it requires a low Courant number. Usually, for boundary cells we have to apply the nonlinear approach, especially for lip shocks. Of course, extraction of the barrel shock waves, lip shocks, and bow shocks for flight simulation always requires a nonlinear approach.

The algorithm was tested against the exact solution of the following problems: one-dimensional flow from a point source, two-dimensional Prandtl–Meyer rarefaction flow, a flow around a wedge, and two-dimensional shock wave reflection from a plate. Comparison was also made to a similar solution for a flow around a cone. For each case, sensitivity to grid variation was studied and the integral conservation law for flow in each cross section was examined. The different tests show that the algorithm achieves high resolution and is very fast and economical, especially with two-dimensional flow simulations. For example, a computation by the two-dimensional K-G code with 100 cells in a cross section leads to an error of less than $\sim 0.1\%$. For the jet nozzle flowfield and nozzle plume extending to 50 jet radii, the computation requires only about 60 s on an Indigo III computer workstation.

The same tests were applied to the three-dimensional flow. Note that one-dimensional flow from a point source in a cylindrical coordinate system is a three-dimensional problem if a point origin is not located in the x axis of this system. Of course, this code required
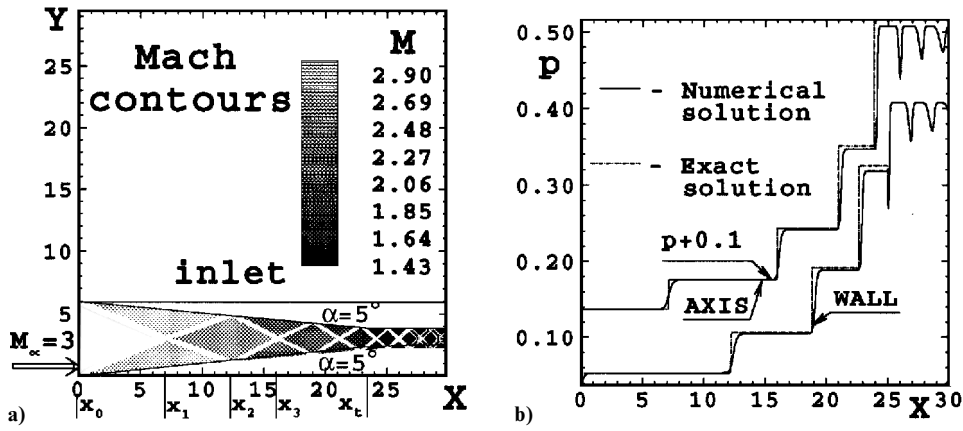
Fig. 2   Comparison of numerical and exact solutions for a two-dimensional wedge-shaped inlet flow.

more time for the computation to reach the given accuracy of less than ~0.1%. The grid $J \times K = 60 \times 10$ provides an accuracy of ~0.3–0.5% for the thrust augmentation along the nozzle wall. These estimates are for the Bluebell nozzle with $n_p = n_c = 4$ and 8 and $\varepsilon \leq 0.3$, $\delta_0 \leq 0.2$. We have used three different grids for numerical comparison of results and have calculated the maximal error of the integral conservation laws for each cross section of the marching scheme in the x direction, $x = x_* + ih_x$, $(i = 1, 2, \ldots, I)$.

An example of such test results is shown in Figs. 2a and 2b. Figure 2a illustrates Mach contours computed by the two-dimensional K-G code of a supersonic flow with $M_\infty = 3$ into a wedge-shaped inlet with angle $\alpha = 5$ deg. The code used 200 cells in each cross section with uniform step h_r. The oblique shock wave at the wedge repeatedly reflects from the symmetry plane and from the wall. The reflected shock waves are inclined at angle β_m. The reflection coordinates and all constant flow parameters at the shock interface are calculated by the exact relationships on oblique shock waves and by simple geometric relationships. This is reached by solving the implicit equation

$$\tan \alpha = \frac{f(\beta_m)/\tan \beta_m}{1 - f(\beta_m)}, \qquad f(\beta) = \frac{2}{k+1}(\sin^2 \beta - M^{-2})$$

with the help of the Newton iterations relative to the shock wave angle β_m. Pressure distributions computed by the exact method and the two-dimensional K-G code are shown in Fig. 2b along the plane of symmetry and along the wall. The error of the numerical scheme is no more than ~0.5% up to one to four reflections from both walls.

Note that in Fig. 2 the wedged wall transforms to the plate that is parallel to the upstream flow at the inlet. Prandtl–Meyer rarefaction waves are formed at the section $x = x_t$, as indicated in Fig. 2a. These waves interact with reflected shock waves. In the sections $x > x_t$, we did not perform analytical computations because of the complexity of the formulation (see Ref. 10). The oscillatory pressure distribution downstream of the section at $x = x_t$ shows the influence of this interaction. The oscillatory amplitude decreases downstream because of reflected shock waves being weakened by the rarefaction waves. The coordinate of transformation is defined by the formula $x_d = (h_1 - 1)/2 \tan \alpha$, where h_1 is an inlet height. For this case $h_1 = 3$, $\alpha = 5$ deg, so that $x_t = 23.5$. The accuracy of the numerical solution increases with increasing flow Mach number, M_∞ or the wedge angle α.

Boundary Layer Patankar–Spalding's Numerical Method

This algorithm is based on a six-point second-order, implicit finite-difference scheme for the two-dimensional steady compressible boundary layer numerical solution. This method and algorithm is described by Patankar and Spalding.[8] The energy and momentum equations are cast in terms of the Mises variables (x, ψ), where ψ is a streamline function. This SPALD-2 code is very fast and convenient for nozzle-jet numerical simulations and for examination of different turbulence models. We used this code for two-dimensional problems and modified it for three-dimensional boundary layer problems. The

subsonic and transonic flow is defined by the sequential iterations with external flow as we described in a prior section. In the supersonic region, we use this code as a subroutine in combination with two- and three-dimensional K-G codes. The appropriate iterations were conducted in each cross section $x = $ const and the defined equivalent nozzle boundary. For a supersonic flow into a Bluebell nozzle, where $n_c = n_p = n$, there are $2n$ planes of symmetry. Therefore, it is sufficient to compute only between two planes in the interval $(0 \leq \varphi \leq \pi/n)$. In each of these planes, a boundary layer is two dimensional if one ignores second derivatives in the φ direction. Assuming that the three-dimensional boundary layer thickness is $\delta_*(x, \varphi)$ and the friction at the wall is $\tau_w(x, \varphi)$, one can approximate these by the function

$$g(x, \varphi) = \frac{g_0(x) - g_K(x)}{2} \cos n\varphi + \frac{g_0(x) + g_K(x)}{2} \qquad (6)$$

where subscript indices 0 and K correspond to their values in $\varphi = 0$ and $\varphi = \pi/n$ planes of symmetry. In relation, (6) g is either δ_* or τ_w. Comparison with the fully Navier–Stokes equation (NSE) simulation results shows that such an approximation is most effective for $n \leq 4$, $\varepsilon \leq 0.3$, $\delta_0 \leq 0.3$–0.4 and when the nozzle is operated nearly fully pressure balanced (i.e., $p_e \sim p_\infty$). A similar approximation was applied earlier for three-dimensional supersonic flows around blunt bodies. However, the agreement with NSE numerical simulation illustrated in Fig. 5 is better when we have used instead of (6) the approximation in the form

$$g(\xi, \varphi) = \frac{g_0(\xi) - g_K(\xi)}{2} \cos n\varphi + \frac{g_0(\xi) + g_K(\xi)}{2}$$

$$\xi = \frac{x}{x_*} \quad \text{at} \quad x \leq x_* \qquad \xi = \frac{x - x_*}{x_e(\varphi) - x_*} \quad \text{at} \quad x \geq x_* \qquad (7)$$

This result has a very simple explanation. For a corrugated lip-line nozzle edge, approximation (6) requires some extrapolation for the wall shape between the two neighboring petals. Otherwise, we have applied here corresponding values for boundary layer using for this area the nozzle shape, which coincides with the inviscid jet boundary. Approximation (7) does not use any extrapolation but with an increase of petal amplitude ε, the errors of such approximations also quickly increase. Therefore, we had good agreement with a full NSE numerical simulation only for the petal amplitudes $\varepsilon \leq 0.3$.

The turbulent boundary layer theoretical model[8] is based on the Prandtl mixing-length hypothesis, a one-dimensional representative flow near a wall (Couette flow) and the van Driest[11] hypothesis, which introduces an "effective" viscosity near a wall as

$$\mu_{\text{eff}} = \mu + \rho K^2 y^2 [1 - \exp\{-y \sqrt{\tau \rho}/(\mu A_+)\}]^2 \left| \frac{\partial u}{\partial y} \right|$$

where A_+ and K are constants, y is the normal direction to the wall, μ is a laminar viscosity, $\rho K^2 y^2 |\partial u/\partial y|$ is a turbulence viscosity, and the latter is "damped" near the wall in an exponential fashion.

Thrust Calculation

In accordance with the traditional thrust definition, introduce P and the corresponding nondimensional value T as

$$P = \int_{\Sigma_e} (\rho_e u_e^2 + p_e)\, d\Sigma - p_\infty \Sigma_e, \qquad T = \frac{P}{p_0 \Sigma_*} \qquad (8)$$

where subscript indices e, ∞, 0, and $*$ are assigned to the nozzle exit cross section, ambient, total, and critical (in a throat) parameters, respectively. Σ_* is a throat area. The integrand expression in (8) is called an impulse function.[12] Such a definition is introduced for rocket motors, but it does not take into account vehicle drag, and it assumes the same shape of the external and internal vehicle surfaces. Therefore, it only approximates the real vehicle net thrust. Nevertheless, we use this definition for estimation of the nozzle shape variation influence on the thrust. The ideal thrust of a nozzle is determined from the quasi-one-dimensional approximations assuming an isentropic perfect gas. These are simple formulas, available in many textbooks—for example, Ref. 12. Let us define $T_{id}(k, \text{NPR})$ as the thrust of the ideal nozzle and ΔT_{id} as the thrust augmentation from the supersonic (divergent) part of such a nozzle. These values are calculated with the base formula (4.33) for T_{id} from the textbook[12]:

$$T_{id}/(p_0 \Sigma_*) = k\sqrt{[2/(k-1)][2/(k+1)]^{(k+1)/(k-1)}}$$

$$\times \sqrt{1 - (p_\infty/p_0)^{(k-1)/k}} + (\Sigma_e/\Sigma_*)[(p_e/p_0) - (p_\infty/p_0)] \quad (9)$$

In accordance with (9), the thrust reaches the maximal value for the designed nozzle $p_e = p_a$. This value is completely defined by specific heat ratio k and pressure ratio $\text{NPR} = p_0/p_\infty$. We define the thrust T and its augmentation ΔT directly by integration of the impulse function from the inlet cross section I_0 and the difference between pressure and friction along the nozzle wall. The integral of the impulse function at the nozzle exit, taking into account the boundary layer, allows us to estimate the integral error of the applied numerical scheme. Thus, the thrust for a single design is calculated by using the preceding nondimensional variables as

$$T = B(I_0 + I_1) - (p_\infty/p_0) \times (\Sigma_e/\Sigma_*)$$

$$B = (k/\pi)[2/(k+1)]^{k/(k-1)}$$

where

$$I_0 = \int_0^{x(\varphi)} \int_{r_0}^{r_e} \int_0^{2\pi} p\left(1 - \frac{k}{2} M_w^2 c_f \sin\alpha\right) r\, dx\, dr\, d\varphi$$

$$I_1 = I(x_0) = \int_0^{r_0} \int_0^{2\pi} (p + \rho u^2) r\, dr\, d\varphi$$

and

$$\Delta T = T - T_* \qquad (10)$$

where T_* is the thrust of a convergent nozzle part.

Numerical Simulation Results

Using the approach and numerical schemes described in the prior sections, we conducted simulations of the internal flow in the Bluebell nozzles and the exhaust jet. These simulations included a wide diversity of nozzle geometries, in particular, variation of the petal and corrugation coefficients ε, δ_0, their frequencies n_p and n_c, exit Mach numbers M_e, and baseline nozzle variation (i.e., conical and optimal axisymmetric nozzles). An optimal nozzle provides maximum thrust for the fixed convergent length part.

We concentrated on a baseline nozzle for shock-free flow with $M_e = 1.5$ because we had obtained acoustic data for this nozzle. Figure 3 illustrates Mach contours for the four-petal nozzle with $\varepsilon = 0.7$ and $\delta_0 = 0.2$. Here, there are two meridional planes of flow symmetry: $\varphi = 0$ and 45 deg. They are limited by the axis of symmetry, nozzle boundary, and inviscid jet boundary from the nozzle throat at $x = 0$ to the end of the fourth barrel at $x = 10$. These cross sections are located at the nozzle throat ($x = 0$), two at internal nozzle cross sections, $x_2 = 1$ and $x_3 = 2.5$, close to the nozzle exit,
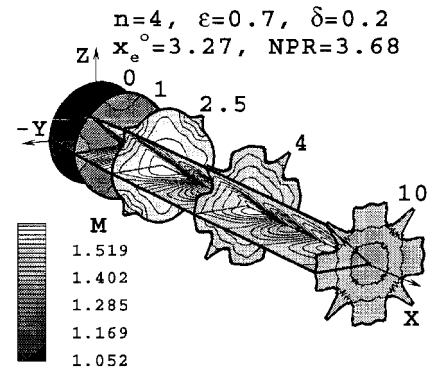

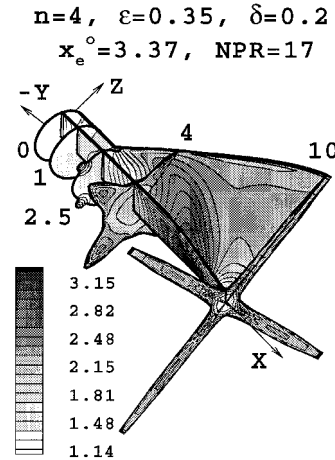Fig. 3 Mach contours in the planes of symmetry and in the five cross sections.

Fig. 4 Mach contours in the planes of symmetry and in the five cross sections.

$x_4 = 4$, and at the end of the computed interval $x_5 = 10$. This cross section is located at the end of the first jet barrel, i.e., where the internal barrel shock wave meets the x axis. Note that in this section we define an origin $x = 0$ not at the subsonic inlet as in the prior sections but at the nozzle throat. At the top of Figs. 3 and 4, the amplitude δ corresponds to its maximal value δ_0. Apparently, the round shape deforms to a round-rectangular shape and further, just downstream of the nozzle exit, it takes a shape similar to petals or a flower: a round part transforms to rectangular and from rectangular to almost triangular. The petals become sharper, which promotes the formation of streamwise vortices. The streamwise vortices improve mixing of the jet flow.

Figure 4 shows development of cross-section Mach contours and jet shape in the planes of symmetry for $\text{NPR} = 17$. For underexpanded jets, such mixing intensification increases, which is expected. The flow through the "gaps" between petals penetrates into ambient air, forming shapes like that of an ear and at the nozzle exit, $x_4 = 4$, the cross section has a butterfly shape with streamwise vortex flow into its wings. The closed Mach contours show the existence of vortical flow. Near the end of the first barrel, the cross section transforms to an X shape. Calculations with other Bluebell nozzle geometries produce similar results.

Unfortunately, we could not simulate three-dimensional mixing layers effectively and observe formation, development, and destabilization of the vorticities starting from the nozzle exit and moving downstream in the jet exhaust. For this, we need to use a large-eddy simulation approach with the correspondent code. However, even for two-dimensional problems such computational work is very expensive.

The main numerical results concerning thrust optimization are represented in Fig. 5, which shows the ratio of the Bluebell nozzle-first embodiment relative to the baseline nozzle thrust, T_n/T_0, vs nozzle geometric parameters. All comparisons are performed for exhaust Mach number $M_e = 1.5$. There are several curves that illustrate the contribution of different nozzle geometric factors to the thrust: viscous effects, petals, and corrugations. As we have
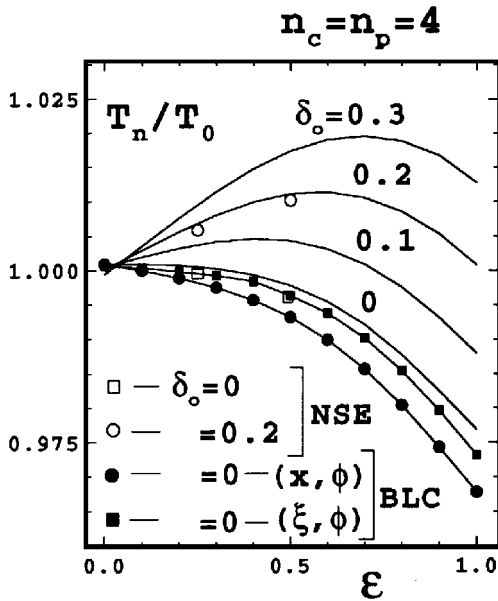
Fig. 5   Thrust ratio of the Bluebell and baseline nozzles.

Table 1   Nine tested nozzles and their geometric parameters

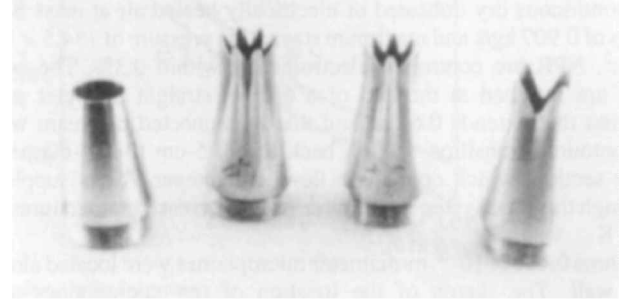| N	1	2	3	4	5	6	7	8	9
n	8	8	8	8	4	4	0	8	0
$\tilde{\varepsilon}$	0.23	0.23	0.38	0.15	0.45	0.45	0	0.23	0
δ_0	0.20	0.00	0.00	0.00	0.20	0.00	0	0.10	0

Fig. 6a   Baseline round and Bluebell nozzles.
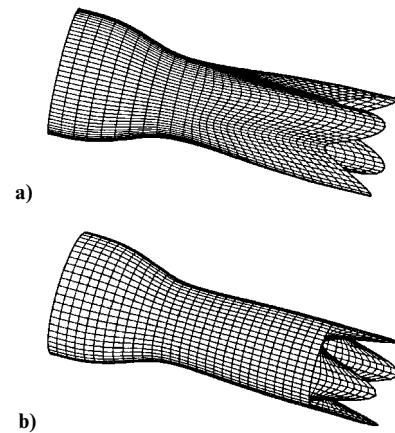

Fig. 6b   Eight-petal Bluebell nozzle in the SAJF.

Fig. 7   Second embodiment of the four-petal Bluebell nozzle.

noted, the agreement between full NSE numerical simulation results shown by the open circles and squares, and boundary layer correction (BLC) shown by the filled circles and squares, are better for the BLC approach using approximation (7).

The parametric intervals used are limited by restrictions in the numerical scheme following from the condition $M_x > 1$. The dependence of the thrust on corrugation coefficient and frequency is found to be more significant than from petal values. The influence of the petal length (ε) is nonmonotonic; for small values, $\delta_0 < 0.025$, the thrust reduces with ε increasing, but it increases with ε when $\delta_0 > 0.025$ and $\varepsilon < \varepsilon_m$. These curves represent the maximum values achieved by Bluebell nozzle geometry. Several factors influence the behavior of these curves. The first occurs from increase of the nozzle length with a corresponding "effective" Mach number increase at the exit. Of course, for the case $\varepsilon > 0$ the term "exit" is a conditional understanding and Mach number can change significantly along the exit lip line. On the one hand, a lateral flow reduces a pressure at the wall; on the other hand, it reduces the effective boundary layer thickness δ_*. The flow expands into the nozzle's channels, and this creates additional thrust by hydrodynamic pressure on the "lateral sides" of such channels.

Another dependence is observed for Bluebell nozzle-second embodiment. The thrust ratios are similar to those observed for the prior case. There is some thrust loss from the friction of the gas flow with the almost horizontal additional sheet with the petals. However, this thrust loss is insignificant and does not exceed 1–2%. This is much less than thrust losses encountered for nozzles described in Refs. 3 and 13 that suppress noise.

The general conclusion obtained from the numerical simulation is that there is an optimum set of geometric parameters, which provide a maximum thrust exceeding the usual round nozzle thrust. The influence of such nozzle shape variation on jet noise is examined in the next section.

Acoustic Data

Experimental Approach

The Bluebell nozzle design takes into account all theoretical and numerical understanding discussed above. Nine different nozzles were made, including the baseline round nozzle. The list of these nozzles assigned by numbers 1–9 is represented in Table 1, along with their geometric parameters $n = n_p = n_c$, ε, δ_0. In Table 1, nozzle 7 is the round convergent baseline nozzle and nozzle 9 is the round convergent–divergent baseline nozzle. Four of them are shown in Fig. 6a.

All nozzles have throat radius $r_* = 0.0165$ m. The round nozzle has exit radius $r_e^0 = 0.0176$ m. The Bluebell nozzles have exit radii defined by Eq. (2b). The length of the convergent part of all nozzles

is $x_* = 0.0522$ m, and the entire length of the baseline round nozzle is $x_e^0 = 0.108$ m. All Bluebell nozzles tested were made on the base of the second embodiment with use of the additional sheets. Their lengths are varied from the baseline nozzle by an additional 0.025–0.028 m (1.0–1.1 in.) depending on the geometric parameters selected for the nozzle. The internal surfaces of the two four-petal Bluebell nozzles are shown in Figs. 7a and 7b with the amplitude of corrugation $\delta_0 = 0.2$ (**a**) and without corrugation $\delta_0 = 0$ (**b**). In both cases, the petal amplitude is the same, $\tilde{\varepsilon} = 0.45$. Note that for the second embodiment the petal amplitude definition, $\tilde{\varepsilon}$, differs from value ε in our theory in accordance with formula (1c). The abscissa x_e of a nozzle lip-line edge for the second embodiment is calculated by the formula

$$x_e = x_e^0 + \tilde{\varepsilon}[1 + \cos(n_p\varphi)] \qquad (11)$$

so that the relationship between these "petal amplitudes" is $\tilde{\varepsilon} = x_e^0 \varepsilon$, and the abscissas are nondimensional ($\tilde{\varepsilon} = 3.27\varepsilon$).

The experiments were conducted in the Small Anechoic Jet Noise Facility (SAJF) at the NASA Langley Research Center. Figure 6b shows part of this facility with Bluebell nozzle 1. The interior dimensions of the facility within the wedge tips are 3.05 × 3.96 × 2.44 m high. The anechoic treatment absorbs at least 99% of incident sound at frequencies greater than 150 Hz. The air system provides a supply of continuous dry unheated or electrically heated air at mass flow rates of 0.907 kg/s and maximum stagnation pressure of 154.5 × 10⁶ N/m². NPR are controlled electronically within 0.3%. The nozzles are fastened at the end of a 63.5-m straight diameter pipe section that extends 0.61 m and that is connected upstream with a contoured transition section back to a 7.5-cm (3 in.)-diameter pipe section, which contains a flow straightener. Air is supplied through this pipe system to the nozzle and can reach temperatures of 811 K.

Three 0.635×10^{-2}-m-diameter microphones were located along the wall. The sketch of the location of the microphones and nozzle-jet system is shown in Fig. 8a. All dimensional values presented for microphone locations are $\theta_1 = 91.1$ deg, $\theta_2 = 125.7$ deg, $\theta_3 = 145$ deg, $S_1 = 1.8$ m (70.75 in.), $S_2 = 3.08$ m (121.375 in.), $S_3 = 2.18$ m (86.125 in.); $h = 0.254$ m (10 in.). The data from these microphones were low-pass-filtered at 100 kHz, amplified, and digitized before being sent to the computer for storage and analysis.

Experimental Results

All nozzles shown in Table 1 were tested at both supersonic and subsonic conditions. In the supersonic regime, the nozzles were operated slightly underexpanded at NPR = 4.0 and jet total temperature $T_j = 450$ K. This corresponds to a fully expanded jet Mach number of 1.56 with a corresponding exit velocity of 530 m/s. All nozzles, except convergent nozzle 7, were designed for fully expanded Mach number $M_e = 1.5$. In the subsonic regime, the nozzles were operated at NPR = 1.27 and at a jet total temperature of 554 K. This corresponds to exhaust Mach number $M_e = 0.6$ with corresponding exit velocity 274 m/s. At either supersonic or subsonic nozzle operating conditions, the nozzles were conducted dimensionally to produce the same ideal thrust.

Because of the small size of the nozzles of Table 1, it is not possible to display acoustic data in terms of the perceived noise level metric. Instead, we show comparative results in terms of the measured overall sound pressure level, and then we show comparative narrow band spectra of those nozzles of most interest.

Figures 8b and 8c show the overall sound pressure level results for all nozzles. Figure 8b compares results at the supersonic condition and Fig. 8c compares those at the subsonic condition. In the supersonic regime, the overall levels are shown as differences relative to that measured from the baseline convergent–divergent nozzle with design exhaust Mach number $M_e = 1.5$. In the subsonic regime, the reference nozzle is the baseline convergent nozzle. In both the supersonic and subsonic regimes, the reference nozzles produced maximum sound radiation at angle $\Psi = 145$ deg. Figure 8b shows that all nozzle concepts produced various levels of noise reduction at the peak radiation angle and even at $\Psi = 91.1$ deg. The noise reduction at $\Psi = 125.7$ deg was the least, even indicating levels above the baseline nozzle. In all cases, those nozzles with corrugations displayed the best acoustic performance (i.e., nozzles 1, 5, and 8). Also, increasing the nozzle perimeter leads to improved levels of noise reduction.

Figure 8c indicates that most nozzle configurations actually produced more noise than the baseline convergent nozzle. The only one showing some promise is nozzle 1. The results shown in Figs. 8b and 8c are not surprising. In the supersonic regime, noise is heavily driven by Mach wave emission, where it is generally good practice to select a suppression concept that enhances mixing. However, we now have observed the following anomalous behavior: nozzle 1 works well in both flow regimes. Thus, it is important that we show details of the narrow band spectra for this nozzle to see where the noise reduction occurs.
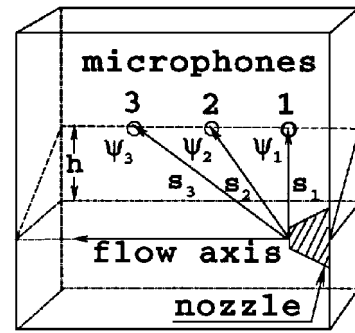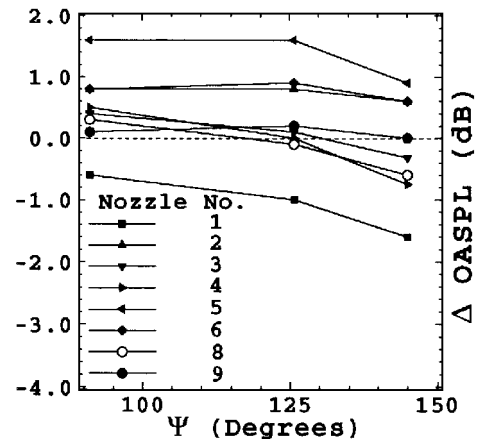

a) Mutual location of the microphones, nozzle, and jet
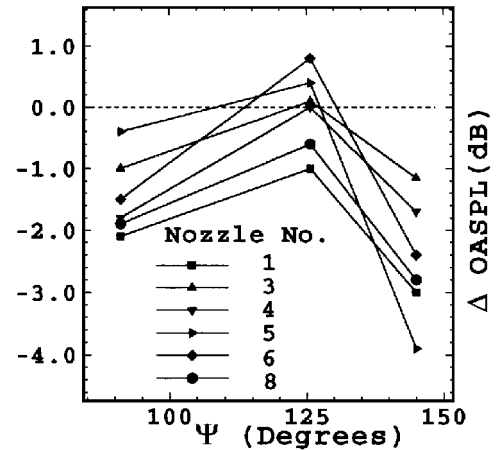
b) Overall pressure level differences vs angle Ψ

c) Overall pressure level differences vs angle Ψ

Fig. 8 Location of microphone and nozzle and overall sound pressure levels.

Figures 9a and 9b show, respectively, narrow band spectra for angles $\Psi = 91.1$ and 145 deg to the nozzle inlet. These spectra are acquired at the supersonic condition. All spectra were computed from digitized time records with a 2K fast Fourier transform, which provides a spectral resolution of 100 Hz. From Fig. 9a, one clearly can observe the presence of screech and broadband shock noise in reference nozzle 9. This is expected because of operation at the slightly underexpanded condition. Note, however, that Bluebell nozzle 1 has significantly reduced shock noise, but it is difficult to determine whether the high-frequency range contains shock noise above 20 kHz for this nozzle. The spectrum in Fig. 9b shows that the noise reduction achieved in the peak radiation direction occurs over the entire spectral range.
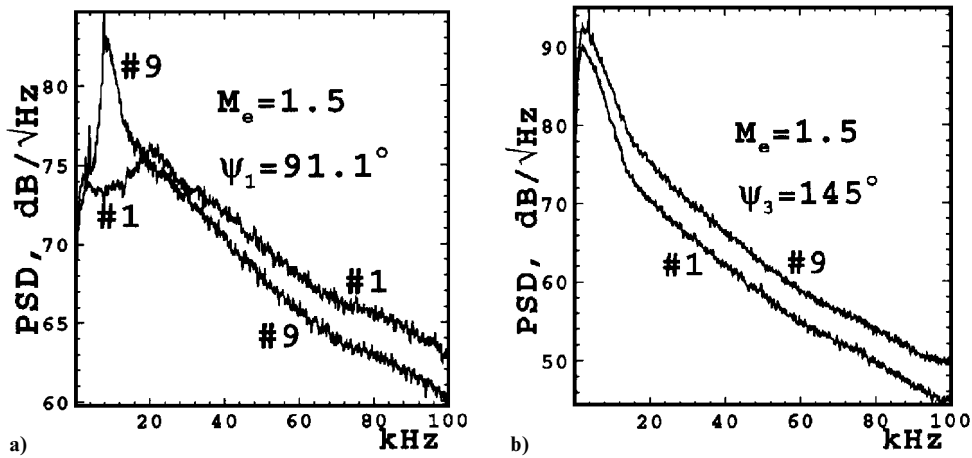
Fig. 9   Acoustic power spectral density vs frequency.

Discussion and Conclusions

In this paper, we have examined both the thrust and noise performance of several round axisymmetric nozzles designed with chevrons and corrugations and have made comparisons to reference baseline convergent–divergent $M_e = 1.5$ and convergent nozzles. All nozzles with chevrons and corrugations were designed as convergent–divergent nozzles with exhaust Mach number $M_e = 1.5$. The thrust calculations were performed by using the Krayko–Godunov numerical scheme (Euler based) both with and without boundary layer correction. Additional thrust calculations were performed with a full Navier–Stokes code with a k-ε turbulence model for select cases.

The thrust calculations for the supersonic regime demonstrated that Bluebell nozzle 5, with $\delta_0 = 0.2$ and $\varepsilon = 0.45$ (see Fig. 5), actually has augmented thrust in the range of 1%. The noise data for this nozzle (i.e., Fig. 8b) exhibit a reduction of noise of nearly 4 dB. The thrust calculations also indicated that even better aeroperformance could be obtained at greater values of the corrugation amplitude δ_0 and also with an increase in nozzle perimeter, as reflected through the parameter ε. The noise results also showed that increased suppression is obtained with increasing values of δ_0 and ε. Unfortunately, we have not constructed such a model nozzle, nor have we yet predicted or measured the turbulent flowfield to further confirm these results. This is being addressed at this time. The thrust calculations also revealed that standard methods usually applied to account for boundary layer thickness with a Euler solver provide misleading results similar to those obtained from Navier–Stokes simulations (see Fig. 5).

The subsonic acoustic results were disappointing but not entirely unexpected. They demonstrate what we have known for a long time. Noise reduction is very difficult to achieve at low exhaust velocities. At high velocities, noise reduction is achieved simply through enhanced mixing, although, in general, it comes as a tradeoff with aeroperformance. Thus, the Bluebell nozzle without ejector is an exception. With an ejector, one expects even better aeroperformance and noise suppression from the Bluebell nozzle, and it may even be possible to achieve this in the subsonic regime. As stated in the introduction, one needs to investigate the turbulent acoustic source to properly optimize the nozzle geometry, particularly in the subsonic regime.

References

[1]Seiner, J. M., and Krejsa, E. A., "Supersonic Jet Noise and the High Speed Civil Transport," AIAA Paper 89-2358, 1989.

[2]Presz, W. M., Jr., "Mixer/Ejector Noise Suppressors," AIAA Paper 91-2243, 1991.

[3]Seiner, J. M., and Gilinsky, M. M., "A Bluebell Nozzle for Improving the Mixing of Exhaust Jets with Ambient Air," Invention Disclosure, NASA Case LARC-15215-1, 1993.

[4]Seiner, J. M., and Gilinsky, M. M., "Nozzle Thrust Optimization While Reducing Jet Noise," CEAS/AIAA Paper 95-149, 1995.

[5]Loitzansky, L. G., *Mechanics of Liquid and Gas*, Nauka, Moscow, 1973.

[6]Dash, S. M., Sinha, N., Madabhushi, R. K., Lee, R. A., York, B. J., and Hosangadi, A., "Progress in the Unsteady Simulation of Jet Flowfield," AIAA Paper 93-1921, 1993.

[7]Molvik, G. A., and Merkle, C. L., "A Set of Strongly Coupled, Upwind Algorithms for Computing Flows in Chemical Nonequilibrium," AIAA Paper 89-0199, 1989.

[8]Patankar, S. V., and Spalding, D. B., *Heat and Mass Transfer in Boundary Layers*, CRC Press, Cleveland, OH, 1968.

[9]Godunov, S. K., Zabrodin, A. V., Ivanov, M. Y., Krayko, A. N., and Prokopov, G. P., *Numerical Solution of Multidimensional Problems of Gas Dynamics*, Nauka, Moscow, 1976.

[10]Chernyi, G. G., *Gas Flow of High Supersonic Velocity*, Fizmatgiz, Moscow, 1959.

[11]Van Driest, E. R., "On Turbulent Flow Near a Wall," *Journal of the Aeronautical Sciences*, Vol. 23, No. 2, 1956, p. 1007.

[12]Shapiro, A. H., *The Dynamics and Thermodynamics of Compressible Fluid Flow*, Vol. 1, Ronald, New York, 1953.

[13]Seiner, J. M., "Advances in High Speed Jet Aeroacoustics," AIAA Paper 84-2275, 1984.

S. Glegg
Associate Editor